Palaeogeography, Palaeoclimatology, Palaeoecology 516 (2019) 1–10

Contents lists available at ScienceDirect

Palaeogeography, Palaeoclimatology, Palaeoecology

journal homepage: www.elsevier.com/locate/palaeo

# Frequent euxinia in southern Neo-Tethys Ocean prior to the end-Permian biocrisis: Evidence from the Spiti region, India

Alan Stebbins[a,*], Jeremy Williams[b], Michael Brookfield[a], Steven W. Nye Jr[a], Robyn Hannigan[a]

[a] School for the Environment, University of Massachusetts Boston, Boston, MA 02125, USA
[b] Department of Geology, Kent State University, Kent, OH 44242, USA

ARTICLE INFO

*Keywords:*
Pyrite
Framboid size distributions
Microbial sulfate reduction
Sulfur isotopes
End-Permian mass extinction

ABSTRACT

In this study, we reconstruct water-column oxygen availability during the deposition of Late Permian shales (Wuchiapingian to approximately early Changhsingian) using the geochemistry and morphology of sedimentary pyrite ($FeS_2$). Deposition of the shales occurred prior to the end-Permian mass extinction within the southern Neo-Tethys Ocean (Spiti region, Himachal Pradesh, India). We found that the variability of pyritic sulfur to organic carbon ($S_{pyr}/C_{org}$) and the pyritic sulfur isotopic composition ($\delta^{34}S_{pyr}$) did not record changes in oxygen availability at Spiti sections. This was due to the removal of original pyritic sulfur by modern oxidative weathering and diagenetic pyrite formation which overwhelmed the original $\delta^{34}S_{pyr}$ values. However, pyrite framboid size distributions was a reliable recorder of paleoredox conditions. The degree of oxygen limitation varied with multiple transient euxinic events interrupting a predominantly oxic-dysoxic trend near the top of the Gungri Formation upper member (approximately late Wuchiapingian to early Changhsingian). These transient euxinic intervals provide important insight and regional evidence of environmental stress and instability in the southern Neo-Tethys well prior to the end-Permian mass extinction.

## 1. Introduction

The Permian-Triassic (PT) mass extinction, ~252 Ma (Burgess et al., 2014; Baresel et al., 2017), was the largest extinction in Earth's history during which around 90% of marine species and 70% of terrestrial species went extinct (Erwin, 1994). The marine extinction event coincided with the eruption of the Siberian Traps Large Igneous Province and occurred rapidly (~60 kyr; Renne et al., 1995; Burgess et al., 2014; Burgess and Bowring, 2015; Burgess et al., 2017). This was a time of global environmental change including ocean acidification (Payne et al., 2010; Clarkson et al., 2015; Garbelli et al., 2017), ocean anoxia (Wignall and Twitchett, 1996; Isozaki, 1997; Wignall and Twitchett, 2002; Brennecka et al., 2011), eutrophication (Algeo and Twitchett, 2010; Schobben et al., 2015), and global warming (Joachimski et al., 2012; Schobben et al., 2014; Chen et al., 2016). The global extent of specific environmental changes and the exact sequence of events that led to the extinction of marine organisms is still being detangled.

A "superanoxic" ocean was initially proposed as a direct cause of the PT extinction (Wignall and Twitchett, 1996; Isozaki, 1997; Algeo et al., 2010; Algeo et al., 2011). However, further studies refined this hypothesis as much more spatially and temporally complex (e.g., Bond and Wignall, 2010). Globally averaged proxies (e.g., uranium isotopes) suggest at least a six-fold increase in the global extent of oceanic anoxia just prior to the extinction horizon (Brennecka et al., 2011; Lau et al., 2016; Elrick et al., 2017). This expansion continued well into the Early Triassic (Lau et al., 2016). The location and extent of oxygen poor waters likely varied within and between ocean basins prior to, during, and after the extinction event (e.g., Clarkson et al., 2016). Using local proxies to determine where anoxia developed is important to deciphering the causes and mechanisms of the PT extinction.

Relatively few studies have investigated environmental conditions during the multimillion year interval that preceded the extinction interval within the Wuchiapingian (~260–254.1 Ma; Mundil et al., 2004; S.Z. Shen et al., 2011) and earlier parts of the Changhsingian (254.1–251.9 Ma; S.Z. Shen et al., 2011; Burgess et al., 2014). The majority of PT studies focused on environmental change during the extinction interval or the prolonged recovery. However, environmental deterioration may have started well prior to the extinction event itself. Evidence based on quantitative modeling of conodont records suggested environmental stress and instability as early as 1.2 Myr before the extinction event (Wang et al., 2014). Similar evidence for environmental deterioration exists from ammonoid fossils in the Neo-Tethys and Paleo-Tethys (Iran) around 0.7 Myr prior to the extinction event (Kiessling et al., 2018). Biomarker evidence suggested euxinic

* Corresponding author at: 100 Morrissey Blvd., School for the Environment, University of Massachusetts Boston, Boston, MA 02125, USA.
*E-mail address:* alan.stebbins001@umb.edu (A. Stebbins).

https://doi.org/10.1016/j.palaeo.2018.11.030
Received 19 July 2018; Received in revised form 25 November 2018; Accepted 25 November 2018
Available online 28 November 2018
0031-0182/ 

intervals in the eastern Paleo-Tethys (South China) 1.5 Myr prior to the extinction event (Cao et al., 2009). Accompanying intervals of euxinia in the Paleo-Tethys were intervals of increased terrestrial and nutrient input (Xie et al., 2017). Further episodic euxinic intervals during the late Wuchiapingian to early Changhsingian were present on the shallow continental shelf of the Boreal Ocean (East Greenland; Nielsen and Shen, 2004; Georgiev et al., 2015a). Deep water anoxia persisted throughout the Wuchiapingian and Changhsingian in basinal settings of the central Neo-Tethys (Arabian Margin; Clarkson et al., 2016). Similar dysoxic to anoxic conditions existed within the basinal Panthalassa (Japan; Isozaki, 1997; Kato et al., 2002; Wignall et al., 2010). On a global scale, based on uranium isotope data, there was a moderate expansion of anoxia during the middle to late Wuchiapingian (~257–254 Ma) and an intense expansion at the mass extinction interval (~252 Ma; Elrick et al., 2017). Importantly, there was no globally averaged expansion during the Changhsingian (~254–252 Ma; Elrick et al., 2017). The two expanded anoxic intervals corresponded with relatively warmer global temperatures based on conodont oxygen isotopes during the Wuchiapingian and PT extinction compared to the Changhsingian (Chen et al., 2013; Chen et al., 2016).

Using samples from the Spiti region, India, this study seeks to reliably reconstruct the long-term trend in oxygen availability prior to the PT extinction in the southern Neo-Tethys. Our understanding of environmental change that occurred within the Neo-Tethys is limited compared to other PT ocean basins such as the Nanpangiang basin of the Paleo-Tethys. We aim to reconstruct local oxygen availability using framboidal pyrite size distributions, pyritic sulfur concentrations ($S_{pyr}$) and pyritic sulfur-isotopes values ($\delta^{34}S_{pyr}$). Pyrite forms from the products of microbial sulfate reduction (MSR) under oxygen limited conditions (Berner, 1984). Framboidal pyrite represents a syngenetic to early diagenetic phase of pyrite formation while euhedral pyrite is likely a late diagenetic form of pyrite (Canfield et al., 1992). A sample often contains various proportions of both syngenetic and diagenetic pyrite with framboidal pyrite more common under less oxygenated conditions (Bond and Wignall, 2010; Wignall et al., 2010). Framboidal pyrite also varies in diameter with sediments deposited under euxinic bottom-waters containing smaller framboid diameters compared to oxic or dysoxic bottom-waters (Wilkin et al., 1996). In addition, the amount of $S_{pyr}$ per unit organic carbon ($C_{org}$) is higher in euxinic depositional conditions compared to “normal-marine conditions” (Berner and Raiswell, 1983; Leventhal, 1983). Lastly, numerous environmental factors influence whole-rock $\delta^{34}S_{pyr}$ values, but a dominant factor is the availability of seawater sulfate at the zone of MSR (e.g., Gomes and Hurtgen, 2015). Changes in the location of the anoxic-oxic boundary above or below the sediment-water interface can influence the availability of water-column sulfate and the whole-rock $\delta^{34}S_{pyr}$ values. Previous geochemical analyses on the Upper Permian of the Spiti region include: whole-rock elemental concentrations and isotopes (C, N, S, and Pb), organic isotopes (C and N), and trace metals (Ghosh et al., 2002; Shukla et al., 2002; Williams et al., 2012; Williams, 2014; Shen et al., 2015; Ghosh et al., 2016; Mir et al., 2016). These previous analyses characterized changes in productivity, provenance, diagenetic alteration, and oxygen availability. However, work on isolated minerals like pyrite can provide more refined and reliable insight into the Upper Permian redox history of this region.

## 2. Geologic background

The Spiti region is in Himachal Pradesh, India, part of the Lahul & Spiti district in the western Himalayas. Permian-Triassic deposition occurred on the Peri-Gondwana region of the southern Neo-Tethys (Fig. 1A). We sampled the Mud, Attargoo, and Lingti sections (Lingti 2 of Williams, 2014) of Spiti (Fig. 1B; Williams et al., 2012; Williams, 2014). Each section consists of black to silty shales from the upper or Shale member of the Gungri Formation overlain by a 5–10 cm iron-rich layer (ferruginous layer; FL; Garzanti et al., 1996; Bhargava et al., 2004). Above the FL is the lowermost Mikin Formation made up of limestone and shale beds (Fig. 2; Garzanti et al., 1996; Bhargava et al., 2004). The FL allows for regional correlation of the sections and is a sedimentary hiatus. Debate exists on the sub-aerial (Bhatt et al., 1980; Garzanti et al., 1996; Williams et al., 2012) or sub-marine (Bhargava, 2008; Ghosh et al., 2016) nature of the sedimentary hiatus. Furthermore, the presence of phosphate nodules within the Shale member has been interpreted as a consequence of strong upwelling events (Cook and McElhinny, 1979; Garzanti et al., 1996), or alternatively, limited circulation (Bhargava, 2008; Singh, 2012; Ghosh et al., 2016). The Shale member represents mid-shelf deposition (Bhargava, 2008).

The paleontological work on the Gungri Formation is relatively sparse though brachiopods are common in the lower member and crinoids and brachiopods are known from rare siltstone intercalations of the Shale member (e.g., Bhargava, 2008). Our current understanding of the Gungri Formation represents compiled work from multiple sections across the Spiti region (Bhatt et al., 1980; Singh et al., 1995; Garzanti et al., 1996; Bucher et al., 1997; Bhargava, 2008; Ghosh et al., 2016). Briefly, the basal beds of the Mikin Formation, overlying the FL, contain *Otoceras* ammonoid beds indicating a lowermost Triassic age (Krystyn et al., 2004; Krystyn and Orchard, 1996; Orchard and Krystyn, 1998). The FL and the uppermost 1.3 m of the Gungri Formation are considered unfossiliferous (Bhatt et al., 1980). The remainder of the Shale member is defined by the *Cyclolobus* ammonoid zone signifying a Wuchiapingian to lower Changhsingian age (Fig. 2; Bhatt et al., 1980; Singh et al., 1995; Bucher et al., 1997; Bhargava, 2008). Trace fossils (e.g., *Zoophycos*) have also been found at various parts of this interval (Bhargava et al., 1985; Ghosh et al., 2016). The absence of upper Changhsingian fossils in the top Gungri and the sharp contact with the overlying FL indicates that erosion has removed some topmost Permian sediments (Singh et al., 1995; Bhargava and Bassi, 1998; Bhargava, 2008). The FL marks the onset of Lower Triassic Mikin carbonate sedimentation and was probably originally a shale-clast microconglomerate cemented and replaced by pyrite (MB per obs on thin sections). We include Gungri Formation samples leading up to, but not including the FL, and broadly designate the samples as Upper Permian in age with deposition prior to the PT extinction event (Fig. 2). For this study, the sampling resolution and sampling depth below the FL varies by section (Attargoo: 50 cm, Lingti: 300 cm, and Mud: 2800 cm; Fig. 2; Williams et al., 2012; Williams, 2014).

## 3. Methods

For this study, we analyzed 76 samples for framboidal pyrite size distributions, $S_{pyr}$ and $\delta^{34}S_{pyr}$ values. $C_{org}$ values were previously published (Williams et al., 2012; Williams, 2014). We performed all analyses at the School for the Environment's Environmental Analytical Facility at the University of Massachusetts Boston.

### 3.1. Pyritic sulfur and pyritic sulfur-isotopes

We used the chromium reduction method to extract reduced sulfur, assumed to be pyrite, from 0.5 g of powdered whole-rock samples (Canfield et al., 1986). A continuous flow of nitrogen gas purged the apparatus of oxygen. We converted the zinc sulfide precipitate into silver sulfide prior to filtering. We dried the silver sulfide and gravimetrically determined the $S_{pyr}$ concentrations. For $\delta^{34}S_{pyr}$, we weighed 0.3–0.4 mg of silver sulfide into tin capsules with vanadium pentoxide to aid in combustion. We measured the isotope ratios of each sample using a Costech Elemental Combustion System 4010 connected to a Thermo Delta V+ Isotope Ratio mass spectrometer. We use per mille notation relative to Vienna Canyon Diablo Troilite (VCDT) and correct the $\delta^{34}S_{pyr}$ values of each unknown sample to the VCDT scale using three IAEA silver sulfide standards (IAEA-S-1: –0.3‰, IAEA-S-2: +22.67‰, and IAEA-S-3: –32.55‰). As a check standard to monitor accuracy, we use the NBS-127 standard (+21.1‰). The precision of

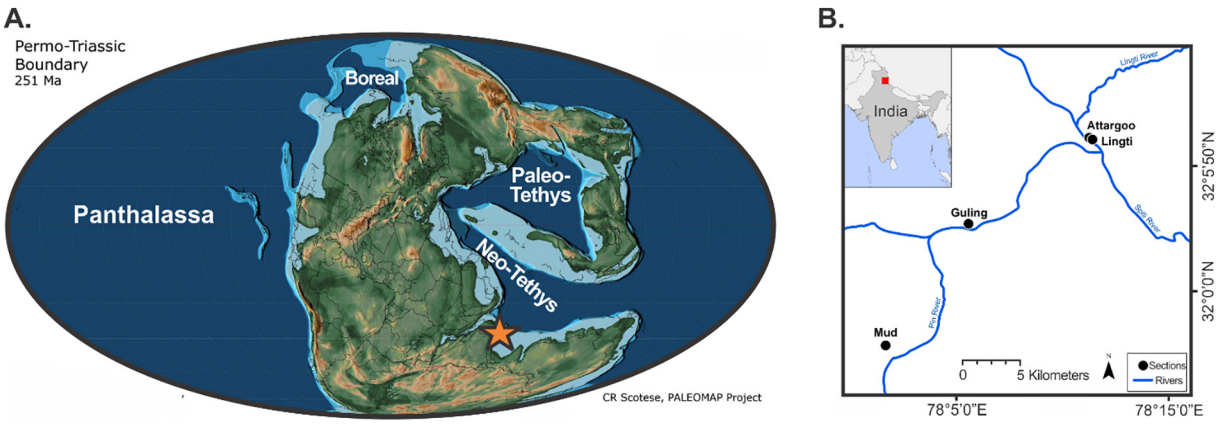


**Fig. 1.** (A) Paleo-location of the Spiti region in the southern Neo-Tethys ocean (star) during the Late Permian (base map modified from Scotese, 2014). (B) Location of the sampled sections (circles) within the Spiti region. Locations of the study sections (circles) within the Spiti region, Himachal Pradesh, India. We analyzed the Attargoo (32° 06′08″N, 78° 11′14″E), Lingti (32° 06′05″N, 78° 11′19″E), and Mud (31° 57′45″N, 78° 01′36″E) sections in this study. Maps made using the ArcGIS program and databases.

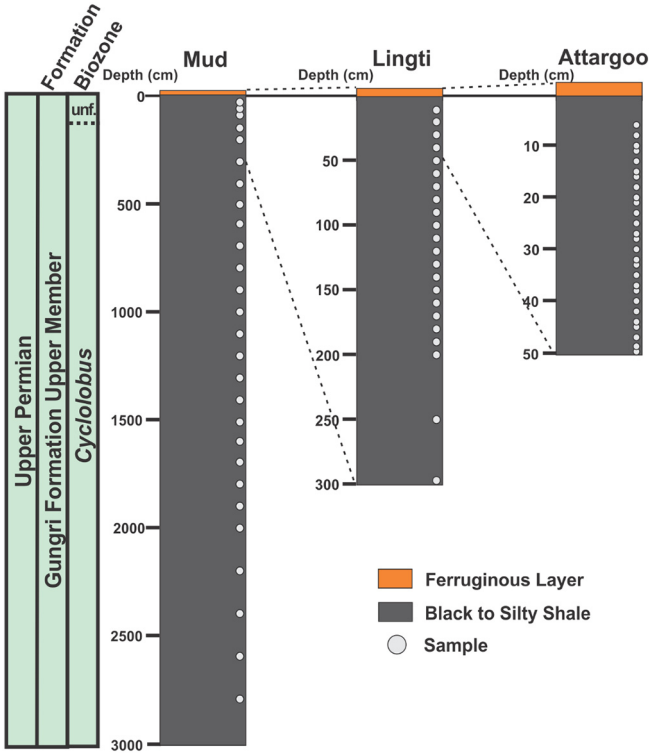


**Fig. 2.** Gungri Formation upper member lithology. Each section consists of black to silty shale capped by a ferruginous layer. We sampled each section at different resolutions below the ferruginous layer (Mud = 2800 cm; Lingti = 300 cm; Attargoo = 50 cm). The distributions of samples are as follows: 27 samples from Mud sampled 30–2800 cm below the FL, 22 samples from Lingti sampled 10–300 cm below the FL, and 27 samples from Attargoo sampled 6–50 cm below the FL. A depth of 0 for all sections marks the base of the FL. The depth scale is not equal between sections as marked by the dashed lines. Abbreviations: unf. = unfossiliferous biozone.

each isotope ratio measurement was < 0.45‰ based on replicate measurements of the IAEA standards.

### 3.2. Pyrite framboid size distributions, abundance, and post-depositional oxidation

We imaged pyritic framboids using a JEOL JSM-6010LA IntouchScope Scanning Electron Microscope (SEM; Fig. 3). We polished whole-rock chips and coated each sample in gold. To identify pyrite based on its unique morphology, we used the backscatter electron mode. Using the built image analysis tools, we measured the diameter of pyritic framboids. Within a sample the goal was to measure at least 100 individual pyrite framboids. This was not always possible due to the abundance of framboidal pyrite within a sample. Based on the amount of pyrite observed while measuring framboidal pyrite diameters, we qualitatively estimated the abundance of framboidal and euhedral pyrite within each sample (none/rare/few/abundant). Using the relation between framboid mean diameter and standard deviation, we proxied paleo-oxygen availability (Wilkin et al., 1996).

We used the spectra results of energy dispersive spectrometry (EDS) on the SEM to determine the degree of oxidative weathering for each sample (Fig. 3). We assigned individual pyrite grains, both framboidal and euhedral, within a sample to an oxidation state based on the relative size of the oxygen and sulfur peaks of the EDS spectrum. We categorized a pyrite grain as not oxidized if the EDS spectrum has a major sulfur peak with a small or absent oxygen peak. Similarly, if there is no sulfur peak and the dominant EDS peak is oxygen, we term the pyrite grain oxidized. If the dominant EDS peak was oxygen but there was still a minor sulfur peak, we categorized the grain as partially oxidized. We then assigned the overall sample an oxidative weathering rank based on the compiled results within the sample.

### 3.3. Statistics

We used Spearman's rho correlation coefficient ($r_s$) to estimate the relation between different variables on the combined datasets of all the three Spiti sections to assess broad depositional trends across the entire region. We gave rank values to the categorical variables (oxidative weathering, framboid frequency, and euhedral frequency) to calculate correlation coefficients. For oxidative weathering, ranks go from oxidized (low) to not oxidized (high). For framboidal and euhedral frequency, ranking goes from less abundant (low) to more abundant (high).

### 3.4. Composite depths

To identify trends for the entire region we produce a composite section. Due to the sparse biostratigraphic data available for the Gungri Formation, the composite is calculated based on the published lengths of the Shale member (Garzanti et al., 1996). This method assumes a constant sedimentation rate for each section. Attargoo has no published thickness, so we assume it is equivalent to Mud. With the short interval sampled at Attargoo (≤50 cm), any error in this assumption does not

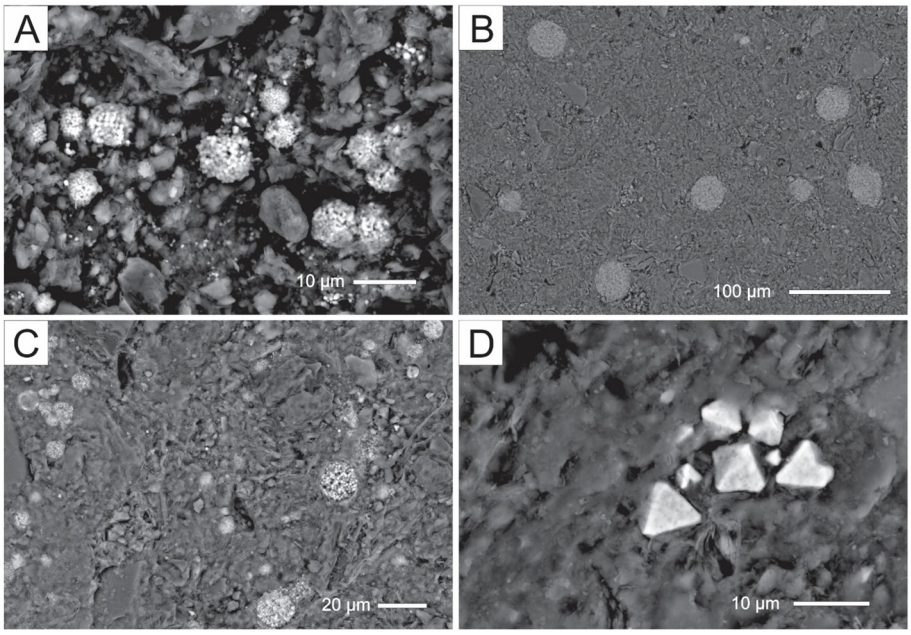


**Fig. 3.** Examples of pyrite from Spiti samples. (A) Unaltered pyrite framboids from Attargoo (PH-2). (B) Large pyrite framboids from Mud (M O-14 m) affected by oxidative weathering. Note that even though the sample has undergone oxidative weathering, the framboid diameter remains easily identifiable. (C) Pyrite framboids from Mud (M O-150 cm) partially affected by oxidative weathering. (D) Euhedral pyrite grains from Attargoo (PI-2).

largely change the relative positioning of samples compared to Lingti or Mud. A composite depth of 0 cm marks the bottom of the FL.

## 4. Results

### 4.1. $S_{pyr}$, $C_{org}$ and $\delta^{34}S_{pyr}$

Overall, all three Spiti sections contained relatively low $S_{pyr}$ concentrations with $\delta^{34}S_{pyr}$ values near 0‰ (Figs. 4–6). Disrupting this pattern were transient intervals of $S_{pyr}$ increases and $\delta^{34}S_{pyr}$ decreases. At Lingti, $\delta^{34}S_{pyr}$ values also increased to $\delta^{34}S_{pyr}$ values well above 0‰. Attargoo contained the highest $S_{pyr}$ concentrations and lowest $\delta^{34}S_{pyr}$ values compared to Mud and Lingti. Specifically, Attargoo's $S_{pyr}$ ranged from 0.04% to 1.5% with a mean of 0.23%, $C_{org}$ ranged from 0.81% to 1.8% with a mean of 1.4%, and $\delta^{34}S_{pyr}$ ranged from −40.2‰ to −0.62‰ with a mean of −12.3‰ (Fig. 4). Lingti's $S_{pyr}$ ranged from 0.04% to 1.1% with a mean of 0.16%, $C_{org}$ ranged from 0.47% to 1.3% with a mean of 0.99%, and $\delta^{34}S_{pyr}$ values ranged from −15.5‰ to +39.2‰ with a mean of +4.8‰ (Fig. 5). Mud's $S_{pyr}$ ranged from 0.05% to 0.20% with a mean of 0.09%, $C_{org}$ ranged from 0.44% to 2.5%

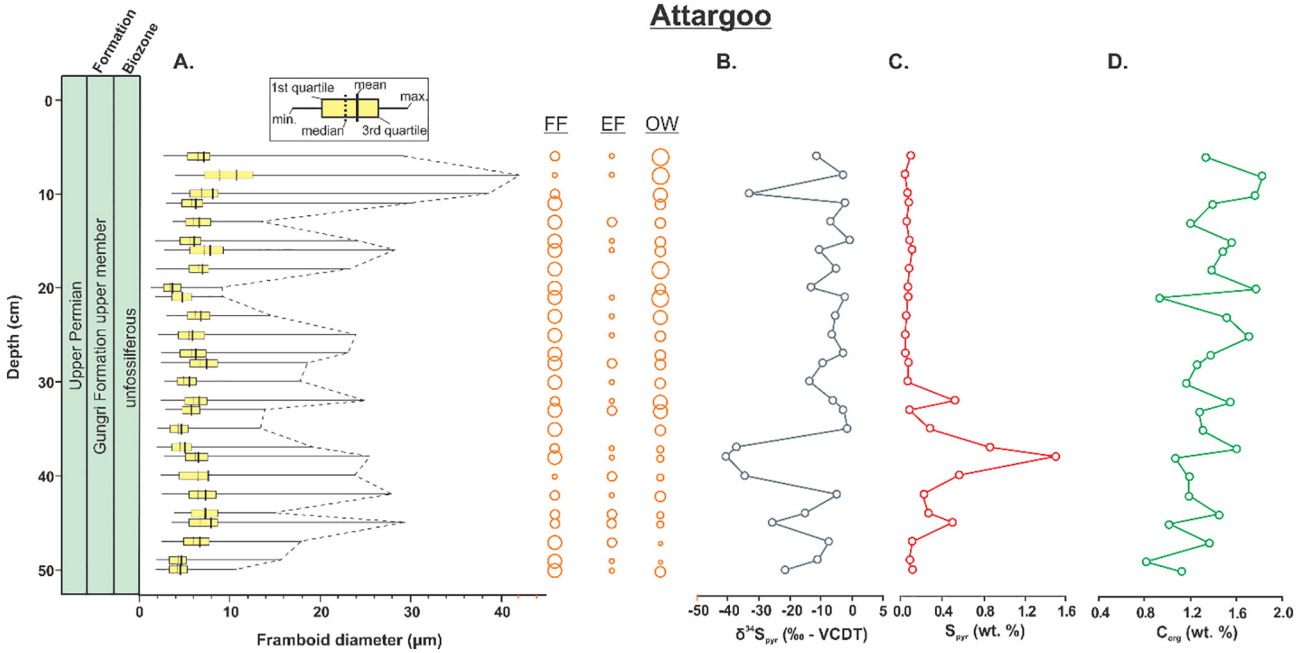


**Fig. 4.** Stratigraphic depth profiles of the Attargoo data. All Attargoo samples were from the unfossiliferous zone above the *Cyclolobus* zone (Bhatt et al., 1980). (A) Pyrite framboid size distributions, framboidal and euhedral pyrite frequency, and degree of oxidative weathering. For the framboid size distributions, the whiskers of the box plots represent the minimum and maximum framboid diameter. The edges of the box represent the first and third quartile of data. The dashed line is the median framboid diameter, and the solid line is the mean framboid diameter. The dashed line on the right whisker connects the maximum framboid diameter of each sample. For the pyrite frequency and oxidative weathering, the larger circles equate to more abundance or oxidative weathering. (B) $\delta^{34}S_{pyr}$ (C) $S_{pyr}$ (D) $C_{org}$ (Williams et al., 2012). Abbreviations: FF – framboid frequency, EF – euhedral frequency, and OW – oxidative weathering.

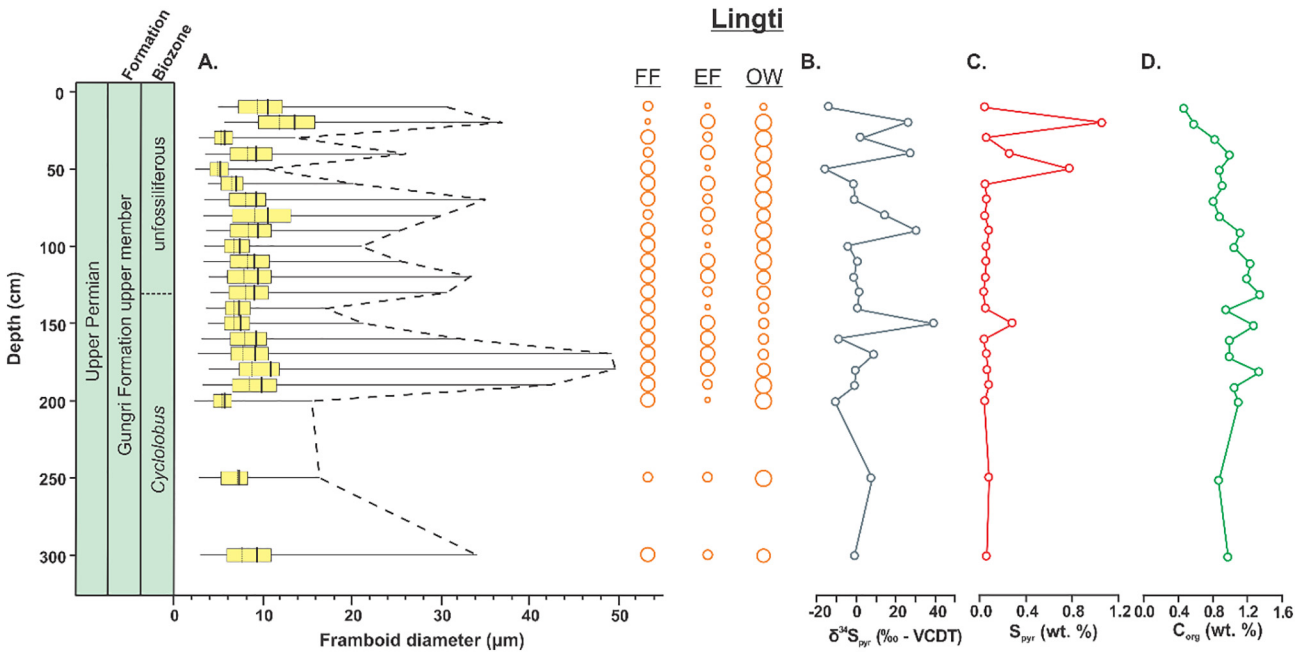


**Fig. 5.** Stratigraphic depth profiles of Lingti data. (A) Pyrite framboid size distributions, pyrite frequency, and oxidative weathering (B) $\delta^{34}S_{pyr}$ (C) $S_{pyr}$ (D) $C_{org}$ (Williams, 2014). See Fig. 4 for a description.

with a mean of 1.3%, and $\delta^{34}S_{pyr}$ valued range from −27.0‰ to +1.6‰ with a mean of −4.0‰ (Fig. 6). Based on the compiled data from all three sections, $S_{pyr}$ contained a weak but significant correlation (the significance threshold was set at 0.05) to $\delta^{34}S_{pyr}$ ($r_s = -0.28$; $p = 0.02$) and framboid frequency ($r_s = -0.23$; $p = 0.04$). $C_{org}$ also weakly but significantly correlated to euhedral frequency ($r_s = -0.40$; $p < 0.001$). For most samples, $S_{pyr}/C_{org}$ ratios were very low and plot well below the "normal-marine regression" line (Fig. 7A). $\delta^{34}S_{pyr}$ values contained significant but weak correlations to mean framboid diameter ($r_s = +0.23$; $p = 0.04$), euhedral frequency ($r_s = +0.33$; $p = 0.004$), $S_{pyr}$ ($r_s = -0.28$; $p = 0.02$), and degree of oxidation ($r_s = -0.47$; $p < 0.001$).

### 4.2. Pyrite framboid size distributions, oxidative weathering, and abundance

The framboidal pyrite morphology dominated most samples with a minor euhedral component. However, the euhedral morphology dominated a few samples, e.g., M-O-28 m and M-O-26 m. The size distributions of pyrite framboids varied throughout each section (Fig. 7B). The mean framboid diameter for Attargoo ranged from 3.7 μm to 10.8 μm with a mean of 6.5 μm (Fig. 4). Lingti ranged from 5.1 μm to 13.5 μm with a mean of 8.7 μm (Fig. 5). Lastly, Mud ranged from 5.3 μm to 13.0 μm with a mean of 7.5 μm (Fig. 6). Common throughout all three sections is some degree of oxidative weathering (Fig. 3). Modern oxidative weathering affected all but two samples (PJ-1 and PJ-2).

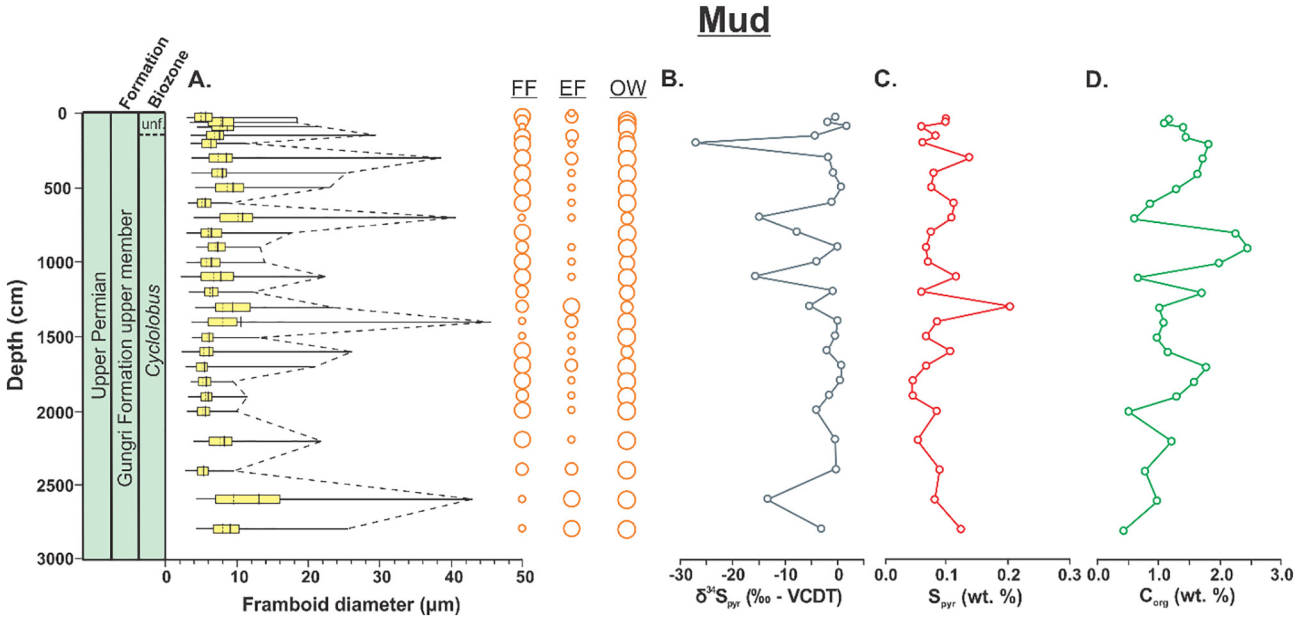


**Fig. 6.** Stratigraphic depth profiles of Mud data. (A) Pyrite framboid size distributions, pyrite frequency, and oxidative weathering (B) $\delta^{34}S_{pyr}$ (C) $S_{pyr}$ (D) $C_{org}$ (Williams, 2014). See Fig. 4 for a description.

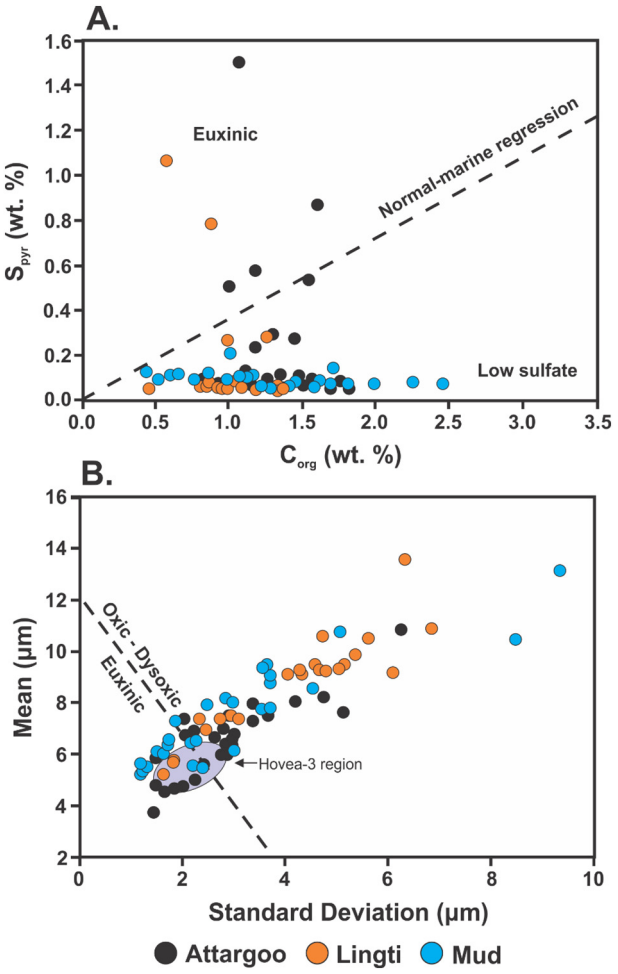


**Fig. 7.** (A) The relation between $S_{pyr}$ and $C_{org}$. The euxinic, normal-marine regression (dashed line), and low sulfate regions are from Berner and Raiswell (1983). The majority of samples plot well below the normal-marine regression due to the post-depositional removal of $S_{pyr}$ by modern oxidative weathering. (B) The relation between pyrite framboid mean diameter and standard deviation. Redox zones defined by Wilkin et al. (1996). The purple ellipse marks the area where Hovea-3 data plot (Bond and Wignall, 2010). (For interpretation of the references to color in this figure legend, the reader is referred to the web version of this article.)

Pyrite from Attargoo was the least oxidized, while pyrite from Mud was the most oxidized.

Mean framboid diameter correlated significantly with the largest framboid size within a population ($r_s = +0.80$; $p < 0.001$) and euhedral frequency ($r_s = +0.51$; $p < 0.001$), and weakly with $\delta^{34}S_{pyr}$ values ($r_s = +0.24$; $p = 0.04$) and framboid frequency ($r_s = -0.36$; $p = 0.002$). Framboid frequency significantly but weakly correlated with mean framboid diameter ($r_s = -0.36$; $p = 0.002$), and $S_{pyr}$ ($r_s = -0.23$; $p = 0.04$). Euhedral frequency significantly correlated with mean framboid diameter ($r_s = +0.51$; $p < 0.001$) and weakly with the largest framboid within a population ($r_s = +0.38$; $p < 0.001$), $C_{org}$ ($r_s = -0.40$; $p < 0.001$), and $\delta^{34}S_{pyr}$ ($r_s = +0.33$; $p = 0.004$).

## 5. Discussion

### 5.1. Oxidative weathering of pyrite and the low $S_{pyr}$ concentrations

Oxidative weathering of pyrite due to post-depositional processes best explains the low $S_{pyr}/C_{org}$ ratios measured in the Spiti samples. Oxidative weathering due to sub-aerial exposure can lower the original $S_{pyr}$ values by converting pyrite to iron oxide. The oxidative weathering process will alter the reconstructed paleo-environmental conditions for pyrite-based proxies, such as $S_{pyr}/C_{org}$ ratios (Leventhal, 1983), compared to unaltered samples (e.g., Georgiev et al., 2015b). Misinterpretation of the low ratios as original depositional values would suggest low sulfate concentrations (Berner and Raiswell, 1984). Based on the number of Spiti samples affected by oxidative weathering, $S_{pyr}$ values and the relative variation between samples are not suitable for reliable paleo-environmental reconstruction.

### 5.2. The driver of $\delta^{34}S_{pyr}$ variation

The sulfur in sedimentary pyrite can be traced to the hydrogen sulfide produced by microbial sulfate reduction (MSR) (Berner, 1970; Berner, 1984). During MSR, microbes use seawater sulfate and organic matter for anaerobic respiration and produce hydrogen sulfide. In turn, pyrite forms from the hydrogen sulfide and captures the isotopic composition of the sulfide pool (e.g., Butler et al., 2004).

The isotopic composition of the sulfide reservoir is strongly influenced by the location of MSR and availability of seawater sulfate (e.g., Gomes and Hurtgen, 2015; Gomes et al., 2016). During MSR, microbes will preferentially reduce the lighter $^{32}S$ isotope of sulfate prior to using the heavier $^{34}S$ isotope. This potentially creates reservoirs of sulfur that, depending on conditions (e.g., open- vs. closed-sulfate system) may contain drastically different isotope values due to Rayleigh fractionation. MSR restricted to sediment porewaters and cutoff from mixing or diffusion of water-column seawater sulfate (closed system) will produce higher $\delta^{34}S_{pyr}$ values than their open-system counterpart. The redox state of the water column is one possible controlling factor on the location of MSR and allows whole-rock $\delta^{34}S_{pyr}$ values to potentially be redox sensitive. However, since the chromium-reduction method produces a whole-rock $\delta^{34}S_{pyr}$ average value, diagenetic pyrite (closed system) can overwhelm the original redox signal. For example, syngenetic pyrite forming under euxinic or anoxic conditions may have relatively low $\delta^{34}S_{pyr}$ values from forming under open-system conditions. If pyrite formation continues during late diagenesis, closed-system dynamics will alter the whole-rock average $\delta^{34}S_{pyr}$ to higher values. Overall, the final proportion of pyrite formed under open- and closed-sulfate systems will largely determine the whole-rock $\delta^{34}S_{pyr}$ value. Importantly, oxidative weathering (Section 5.1) has no fractionation effect on whole-rock average $\delta^{34}S_{pyr}$ values (Ohmoto and Goldhaber, 1997; Seal, 2006; Tuttle et al., 2009; Chi Fru et al., 2016).

For the Spiti region, the $\delta^{34}S_{pyr}$ variation correlated significantly and positively with euhedral abundance ($r_s = +0.33$; $p = 0.004$) and mean framboid diameter ($r_s = +0.24$; $p = 0.04$). However, for each, the amount of variance accounted for was low. This tentatively suggests that the controlling factors for $\delta^{34}S_{pyr}$ variation were the abundance of late diagenetic-closed system pyrite and oxygen availability. However, the abundance of each pyrite morphology was only qualitatively estimated, and so, does not truly quantify the exact proportion of framboidal or euhedral pyrite (e.g., Shen et al., 2016). A method to assess proportions of syngenetic (open system) and diagenetic pyrite (closed system) within a sample, regardless of the morphology, was used at the Nhi Tao, Vietnam PT section (Algeo et al., 2008). A two-endmember mixing model of $\delta^{34}S_{pyr}$ and $S_{pyr}$ was developed which suggests each sample contained proportions of late diagenetic pyrite ($\delta^{34}S_{pyr}$ values = +10‰) and syngenetic pyrite ($\delta^{34}S_{pyr}$ values = −45‰; Algeo et al., 2008). Unfortunately, due to the oxidative weathering that affected $S_{pyr}$ at Spiti sections (Section 5.1), we cannot use this method to assess $\delta^{34}S_{pyr}$ variability.

We conclude the controlling factor on whole-rock $\delta^{34}S_{pyr}$ values at Spiti sections were changing proportions of closed system-late diagenetic pyrite. This is based on the dominance of $\delta^{34}S_{pyr}$ values near 0‰ and that most samples contained a variable amount of different pyrite morphologies. This suggests that for most samples, regardless of water-column oxygen availability, the continued formation of pyrite under

closed-system conditions overwhelmed any remaining redox signature by shifting whole-rock average $\delta^{34}S_{pyr}$ to higher values. Further investigation into the drivers of $\delta^{34}S_{pyr}$ requires either samples unaltered by oxidative weathering or $\delta^{34}S_{pyr}$ measurements of individual pyrite crystals instead of a bulk-pyrite analysis. Most important for this study, the whole-rock $\delta^{34}S_{pyr}$ variability was not reliably recording original redox conditions for the Upper Permian of Spiti.

### 5.3. Upper Permian oxygen availability at Spiti

Pyrite framboid size distribution is a very reliable redox proxy regardless of the variable amounts of oxidative weathering recorded within and between sections in the Spiti region (Section 5.1). The proxy is resistant to weathering diagenesis since the size of the framboid crystal habit remains unchanged even if the elemental composition of pyrite changes (e.g., Wignall et al., 2005). On top of being reliable, pyrite framboid size distributions can differentiate between oxic-dysoxic and euxinic conditions (Wilkin et al., 1996). However, based on the way pyrite forms beneath the anoxic-oxic interface, we must limit any inferences based on framboid size distributions to bottom-water oxygenation conditions. For example, if framboid size distributions suggest an euxinic water column, we cannot determine the height of the anoxic-oxic interface within the water column using only framboid size distributions.

In this study and based on the sampling scheme, pyrite framboid size distributions suggest there were two broad shifts in oxygen availability for the Shale member. The more common occurrence of relatively small framboids between composite depths of −3000 cm and −500 cm suggests that oxygen availability varied mainly between euxinia and oxic-dysoxic lower in the formation (Fig. 8). There was a shift to more consistent oxic-dysoxic conditions between −500 cm to −150 cm. At −150 cm a second shift occurred and interrupting these oxic-dysoxic conditions were further episodic euxinic intervals (Fig. 8). The euxinic intervals became more frequent during the high-resolution sampling within 50 cm of the FL which most likely represented the uppermost Wuchiapingian or lower Changhsingian (Fig. 8; Bhargava, 2008). The Late Permian bottom-waters of Spiti were previously suggested to be anoxic or euxinic based purely on the presence of pyrite framboids (Ghosh et al., 2016). Alternatively, shifts from dysoxia to anoxia and then to euxinia below the FL were suggested based on the trace element geochemistry in the Gungri shales (Williams et al., 2012). However, both studies only analyzed the uppermost 50 cm of the Shale member. Where sampling for this study overlapped the previous studies (Williams et al., 2012; Ghosh et al., 2016), the changing redox reconstructions proposed here were more similar to the variable dysoxic to euxinic range of Williams et al. (2012). Importantly, this study further refined redox variability by using a proxy that remained reliable when varying degrees of oxidative weathering affected the samples and extended conclusions further into the Upper Permian through longer sampled sections.

### 5.4. Regional comparisons and detrimental environmental conditions

Many studies have analyzed pyrite framboid size distributions for various time intervals and regions of the Late Permian or Early Triassic world: eastern Paleo-Tethys (Li et al., 2016; Shen et al., 2016; Wang et al., 2016; He et al., 2017; Huang et al., 2017, and references therein); western Paleo-Tethys (Bond and Wignall, 2010); Boreal (Nielsen and Shen, 2004; Bond and Wignall, 2010; Dustira et al., 2013; Georgiev et al., 2015a; Wignall et al., 2015); Panthalassa (Bond and Wignall, 2010; Wignall et al., 2010; Takahashi et al., 2015); and Neo-Tethys (Wignall et al., 2005; Bond and Wignall, 2010). Of the studies that included samples from the Neo-Tethys, the Guryul Ravine, India section was analyzed only around the PT boundary (Wignall et al., 2005). Alternatively, the Hovea-3, Australia section was analyzed from the Wuchiapingian (~255 Ma; S.Z. Shen et al., 2011) to the Dienerian (~251 Ma; Galfetti et al., 2007) substages (Bond and Wignall, 2010). This partly covered a similar time interval as Spiti deposition, but the sampling resolution was very low, only 12 samples for the multi-million-year interval (Bond and Wignall, 2010).

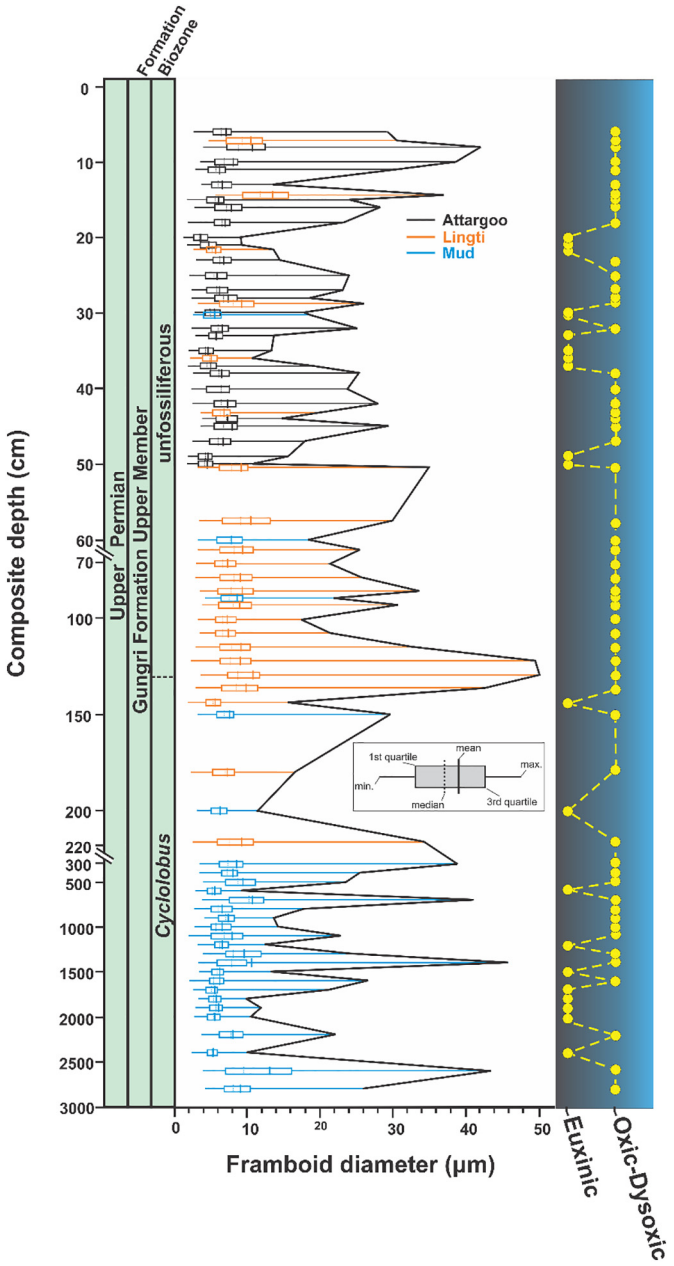


**Fig. 8.** Composite stratigraphic profile of pyrite framboid size distributions. Left panel – framboid size distributions represented by box and whisker plots. If the depth of two samples directly overlapped, one sample was shifted slightly in order to see both. The solid line on the right whisker connects the maximum framboid diameter of each sample. A break symbol marks scale changes. Right panel – reconstructed paleo-redox conditions determined by the framboid size distributions (Fig. 7).

For the same Wuchiapingian to lower Changhsingian interval, the limited data from the Hovea-3 also suggests euxinic and oxic-dysoxic depositional conditions, similar to Spiti samples (Fig. 7B; Bond and Wignall, 2010). The similarity between the different regions tentatively suggests a broader trend across the entire southern Neo-Tethys for the Upper Permian. Important to our study was the significantly higher sample resolution from Spiti sections which allowed for better definition of the long-term redox variability. However, to confidently extend

these trends beyond the Spiti region more data is necessary from other areas of the southern Neo-Tethys such as the Guryul Ravine, India section.

The persistently low oxygen availability and multiple euxinic intervals at Spiti suggests detrimental and unstable environmental conditions in the Upper Permian well prior to the PT extinction. These detrimental conditions support the conclusions from other studies on Upper Permian locations (Nielsen and Shen, 2004; Cao et al., 2009; Georgiev et al., 2015a; Wang et al., 2014; Xie et al., 2017; Kiessling et al., 2018). Specifically, the euxinic intervals could be precursor events to the upward excursions of the chemocline and expansion of euxinia associated directly with the PT extinction (Grice et al., 2005; Kump et al., 2005; Riccardi et al., 2006; Hays et al., 2007; Grasby and Beauchamp, 2009; Algeo et al., 2008; Georgiev et al., 2015b; Schobben et al., 2015; Zhang et al., 2017; Zhou et al., 2017). These euxinic events were also recorded well prior to the PT extinction in other parts of the PT world (Nielsen and Shen, 2004; Cao et al., 2009; Y. Shen et al., 2011; Georgiev et al., 2015a; Wei et al., 2015). The expansion of euxinia and upward excursions of the chemocline associated with the PT extinction were often attributed to environmental change due to the eruption of the Siberian Traps Large Igneous Province including warming temperatures or increased riverine nutrient input (e.g., Zhou et al., 2017). Warmer temperatures, although not as warm as the extinction interval, were also associated with the Wuchiapingian to lower Changhsingian (Chen et al., 2013; Chen et al., 2016). The global expansion of anoxia in the Wuchiapingian (Elrick et al., 2017), and recorded locally at Spiti with euxinic intervals, could similarly relate to warmer temperatures.

With the uppermost Permian likely missing at Spiti, we do not have direct evidence of paleo-environmental conditions at the PT extinction. However, where southern Neo-Tethys uppermost Permian deposits remain, the data suggests both oxygen poor and oxygen rich conditions. For example, the data from the Hovea-3 section suggests anoxic conditions (Bond and Wignall, 2010). Alternatively, the data from the Guryul Ravine, India (Wignall et al., 2005), Gyanyima, Tibet (Garbelli et al., 2016) and Selong, Tibet (Wignall and Newton, 2003) sections all suggest oxic conditions. Slightly further away from the Spiti region, in the central Neo-Tethys, data from the Arabian margin suggested deep water anoxia was prevalent from the Wuchiapingian to the PT extinction (Clarkson et al., 2016). In addition, these anoxic waters likely upwelled onto the mid-slope during the upper Changhsingian and PT extinction (Clarkson et al., 2016). This type of spatial variability exemplifies the regionally complex nature of anoxia and other environmental conditions prior to and during PT extinction.

Nevertheless, the episodic euxinic intervals preserved at Spiti would have stressed aerobic organisms on the continental shelf of the southern Neo-Tethys. This occurred long before the PT extinction interval itself, similar to paleo-environmental reconstruction within the eastern Paleo-Tethys (Cao et al., 2009) and reflected in the fossil records (Wang et al., 2014; Kiessling et al., 2018). This could have created ecosystem conditions which were susceptible and primed for an extinction event, potentially needing only a push past a tipping point. The likely catalyst of global change was the Siberian Traps Large Igneous Province (e.g., Burgess et al., 2017).

## 6. Conclusions

Through analysis of Upper Permian shales from the Spiti region using possible redox proxies of pyrite, we concluded that $S_{pyr}/C_{org}$ and $\delta^{34}S_{pyr}$ did not reflect changes in oxygen availability. $S_{pyr}/C_{org}$ ratios were lower than likely original values due to severe $S_{pyr}$ loss during modern oxidative weathering. Furthermore, the variation in $\delta^{34}S_{pyr}$ reflected diagenetic pyrite formation which overwhelmed any redox signal. Based on pyrite framboid size distributions, the deposition of the Upper Permian shales experienced multiple but transient euxinic intervals which interrupted a long-term oxic-dysoxic trend. Redox conditions preserved at Spiti sections were similar to the Upper Permian of the Hovea-3, Australia section. While not conclusive for the entire Neo-Tethys, when considered together these data suggest a widespread pattern across the southern Neo-Tethys. Lastly, regional stress and deterioration well prior to the end-Permian mass extinction could have provided the necessary susceptibility to enable a final catalyst to set the end-Permian mass extinction into motion for this region.

## Acknowledgments

The authors thank the School for the Environment's Environmental Analytical Facility at UMass Boston (NSF Award # 09-42371; DBI:MRI-RI2; PIs: Dr. Robyn Hannigan and Dr. Alan Christian) for access to analytical instrumentation. A.S. gratefully acknowledges support by the National Science Foundation Graduate Research Fellowship (DGE-1356104), the UMass Boston Chancellor's Distinguished Doctoral Fellowship, and the School for the Environment. Thanks to Thomas Algeo for editorial handling and two anonymous reviewers for constructive reviews of the original manuscript.

## Appendix A. Supplementary data

Supplementary data to this article can be found online at https://doi.org/10.1016/j.palaeo.2018.11.030.

## References

Algeo, T.J., Twitchett, R.J., 2010. Anomalous Early Triassic sediment fluxes due to elevated weathering rates and their biological consequences. Geology 38 (11), 1023–1026.
Algeo, T.J., Shen, Y., Zhang, T., Lyons, T., Bates, S., Rowe, H., Nguyen, T.K.T., 2008. Association of $^{34}$S-depleted pyrite layers with negative carbonate $\delta^{13}$C excursions at the Permian-Triassic boundary: evidence for upwelling of sulfidic deep-ocean water masses. Geochem. Geophys. Geosyst. 9 (4), 1–10.
Algeo, T.J., Hinnov, L., Moser, J., Maynard, J.B., Elswick, E., Kuwahara, K., Sano, H., 2010. Changes in productivity and redox conditions in the Panthalassic Ocean during the latest Permian. Geology 38 (2), 187–190.
Algeo, T.J., Kuwahara, K., Sano, H., Bates, S., Lyons, T., Elswick, E., Hinnov, L., Ellwood, B., Moser, J., Maynard, J.B., 2011. Spatial variation in sediment fluxes, redox conditions, and productivity in the Permian–Triassic Panthalassic Ocean. Palaeogeogr. Palaeoclimatol. Palaeoecol. 308 (1–2), 65–83.
Baresel, B., Bucher, H., Brosse, M., Cordey, F., Guodun, K., Schaltegger, U., 2017. Precise age for the Permian–Triassic boundary in South China from high-precision U-Pb geochronology and Bayesian age–depth modeling. Solid Earth 8, 361–378.
Berner, R.A., 1970. Sedimentary pyrite formation. Am. J. Sci. 268 (1), 1–23.
Berner, R.A., 1984. Sedimentary pyrite formation: an update. Geochim. Cosmochim. Acta 48 (4), 605–615.
Berner, R.A., Raiswell, R., 1983. Burial of organic carbon and pyrite sulfur in sediments over phanerozoic time: a new theory. Geochim. Cosmochim. Acta 47 (5), 855–862.
Berner, R.A., Raiswell, R., 1984. C/S method for distinguishing freshwater from marine sedimentary rocks. Geology 12 (6), 365–368.
Bhargava, O.N., 2008. An updated introduction to the Spiti Geology. J. Paleontol. Soc. India 53 (2), 113–128.
Bhargava, O.N., Bassi, U.K., 1998. Geology of Spiti-Kinnaur, Himachal Himalaya. Mem. Geol. Surv. India 124, 1–210.
Bhargava, O.N., Srivastava, R.N., Gadhoke, S.K., 1985. Zoophycos from the Permian Gungri Member (Kuling Formation), Spiti Valley, Himachal Himalaya. J. Geol. Soc. India 26, 137–140.
Bhargava, O.N., Krystyn, L., Balini, M., Lein, R., Nicora, A., 2004. Revised litho- and sequence stratigraphy of the Spiti Triassic. Albertiana 30, 21–39.
Bhatt, D., Fuchs, G., Prashara, K., Krystyn, L., Arora, R., Golebiowski, R., 1980. Additional ammonoid layers in the Upper Permian sequence of Spiti. Indian Geol. Assoc. Bull. 13, 57–61.
Bond, D.P., Wignall, P.B., 2010. Pyrite framboid study of marine Permian-Triassic boundary sections: a complex anoxic event and its relationship to contemporaneous mass extinction. Geol. Soc. Am. Bull. 122 (7–8), 1265–1279.
Brennecka, G.A., Herrmann, A.D., Algeo, T.J., Anbar, A.D., 2011. Rapid expansion of oceanic anoxia immediately before the end-Permian mass extinction. Proc. Natl. Acad. Sci. U.S.A. 108 (43), 17631–17634.
Bucher, H., Nassichuck, W., Spinosa, C., 1997. A new occurrence of the upper Permian ammonoid *Stacheoceras trimurti* diener from the Himalayas; Himachal Pradesh, India. Eclogae Geol. Helv. 90 (3), 599–604.
Burgess, S.D., Bowring, S.A., 2015. High-precision geochronology confirms voluminous magmatism before, during, and after Earth's most severe extinction. Sci. Adv. 1 (7), e1500470.
Burgess, S.D., Bowring, S., Shen, S.Z., 2014. High-precision timeline for Earth's most severe extinction. Proc. Natl. Acad. Sci. U.S.A. 111 (9), 3316–3321.
Burgess, S.D., Muirhead, J.D., Bowring, S.A., 2017. Initial pulse of Siberian Traps sills as the trigger of the end-Permian mass extinction. Nat. Commun. 8 (164), 1–6.

Butler, I.B., Böttcher, M.E., Rickard, D., Oldroyd, A., 2004. Sulfur isotope partitioning during experimental formation of pyrite via the polysulfide and hydrogen sulfide pathways: implications for the interpretation of sedimentary and hydrothermal pyrite isotope records. Earth Planet. Sci. Lett. 228 (3–4), 495–509.
Canfield, D.E., Raiswell, R., Westrich, J.T., Reaves, C.M., Berner, R.A., 1986. The use of chromium reduction in the analysis of reduced inorganic sulfur in sediments and shales. Chem. Geol. 54 (1–2), 149–155.
Canfield, D.E., Raiswell, R., Bottrell, S.H., 1992. The reactivity of sedimentary iron minerals toward sulfide. Am. J. Sci. 292 (9), 659–683.
Cao, C., Love, G.D., Hays, L.E., Wang, W., Shen, S., Summons, R.E., 2009. Biogeochemical evidence for euxinic oceans and ecological disturbance presaging the end-Permian mass extinction event. Earth Planet. Sci. Lett. 281 (3–4), 188–201.
Chen, B., Joachimski, M.M., Shen, S.-Z., Lambert, L.L., Lai, X.-L., Wang, X.-D., Chen, J., Yuan, D.-X., 2013. Permian ice volume and palaeoclimate history: oxygen isotope proxies revisited. Gondwana Res. 24 (1), 77–89.
Chen, J., Shen, S.Z., Li, X.H., Xu, Y.G., Joachimski, M.M., Bowring, S.A., Erwin, D.H., Yuan, D.X., Chen, B., Zhang, H., Wang, Y., Cao, C.Q., Zheng, Q.F., Mu, L., 2016. High-resolution SIMS oxygen isotope analysis on conodont apatite from South China and implications for the end-Permian mass extinction. Palaeogeogr. Palaeoclimatol. Palaeoecol. 448, 26–38.
Chi Fru, E., Hemmingsson, C., Callac, N., Perez, N., Panova, E.G., Broman, C., El Albani, A., 2016. Atmospheric weathering of Scandinavian alum shales and the fractionation of C, N and S isotopes. Appl. Geochem. 74, 94–108.
Clarkson, M.O., Kasemann, S.A., Wood, R.A., Lenton, T.M., Daines, S.J., Richoz, S., Ohnemueller, F., Meixner, A., Poulton, S.W., Tipper, E.T., 2015. Ocean acidification and the Permo-Triassic mass extinction. Science 348 (6231), 229–232.
Clarkson, M.O., Wood, R.A., Poulton, S.W., Richoz, S., Newton, R.J., Kasemann, S.A., Bowyer, F., Krystyn, L., 2016. Dynamic anoxic ferruginous conditions during the end-Permian mass extinction and recovery. Nat. Commun. 7 (12236), 1–9.
Cook, P.J., McElhinny, M.W., 1979. A reevaluation of the spatial and temporal distribution of sedimentary phosphate deposits in the light of plate tectonics. Econ. Geol. 74 (2), 315–330.
Dustira, A.M., Wignall, P.B., Joachimski, M., Blomeier, D., Hartkopf-Fröder, C., Bond, D.P.G., 2013. Gradual onset of anoxia across the Permian–Triassic Boundary in Svalbard, Norway. Palaeogeogr. Palaeoclimatol. Palaeoecol. 374, 303–313.
Elrick, M., Polyak, V., Algeo, T.J., Romaniello, S., Asmerom, Y., Herrmann, A.D., Anbar, A.D., Zhao, L., Chen, Z.-Q., 2017. Global-ocean redox variation during the middle-late Permian through Early Triassic based on uranium isotope and Th/U trends of marine carbonates. Geology 45 (2), 163–166.
Erwin, D., 1994. The Permo-Triassic extinction. Nature 367 (6460), 231–236.
Galfetti, T., Bucher, H., Ovtcharova, M., Schaltegger, U., Brayard, A., Brühwiler, T., Goudemand, N., Weissert, H., Hochuli, P.A., Cordey, F., Guodun, K., 2007. Timing of the Early Triassic carbon cycle perturbations inferred from new U–Pb ages and ammonoid biochronozones. Earth Planet. Sci. Lett. 258 (3–4), 593–604.
Garbelli, C., Angiolini, L., Brand, U., Shen, S.Z., Jadoul, F., Posenato, R., Azmy, K., Cao, C.Q., 2016. Neotethys seawater chemistry and temperature at the dawn of the end Permian mass extinction. Gondwana Res. 35, 272–285.
Garbelli, C., Angiolini, L., Shen, S.Z., 2017. Biomineralization and global change: a new perspective for understanding the end-Permian extinction. Geology 45 (1), 19–22.
Garzanti, E., Angiolini, L., Sciunnach, D., 1996. The Permian Kuling Group (Spiti, Lahaul and Zanskar; NW Himalaya): sedimentary evolution during rift/drift transition and initial opening of Neo-Tethys. Riv. Ital. Paleontol. Stratigr. 102, 175–200.
Georgiev, S.V., Horner, T.J., Stein, H.J., Bingen, B., Rehkamper, M., 2015a. Cadmium-isotopic evidence for increasing primary productivity during the Late Permian anoxic event. Earth Planet. Sci. Lett. 410, 84–96.
Georgiev, S.V., Stein, H.J., Hannah, J.L., Henderson, C.M., Algeo, T.J., 2015b. Enhanced recycling of organic matter and Os-isotopic evidence for multiple magmatic or meteoritic inputs to the Late Permian Panthalassic Ocean, Opal Creek, Canada. Geochim. Cosmochim. Acta 150, 192–210.
Ghosh, P., Bhattacharya, S., Shukla, A., Shukla, P., Bhandari, N., Parthasarathy, G., Kunwar, A., 2002. Negative $\delta^{13}C$ excursion and anoxia at the Permo-Triassic boundary in the Tethys Sea. Curr. Sci. 83 (4), 498–502.
Ghosh, N., Basu, A.R., Bhargava, O.N., Shukla, U.K., Ghatak, A., Garzione, C.N., Ahluwalia, A.D., 2016. Catastrophic environmental transition at the Permian-Triassic Neo-Tethyan margin of Gondwanaland: Geochemical, isotopic and sedimentological evidence in the Spiti Valley, India. Gondwana Res. 34, 324–345.
Gomes, M.L., Hurtgen, M.T., 2015. Sulfur isotope fractionation in modern euxinic systems: implications for paleoenvironmental reconstructions of paired sulfate-sulfide isotope records. Geochim. Cosmochim. Acta 157, 39–55.
Gomes, M.L., Hurtgen, M.T., Sageman, B.B., 2016. Biogeochemical sulfur cycling during Cretaceous oceanic anoxic events: a comparison of OAE1a and OAE2. Paleoceanography 31 (2), 233–251.
Grasby, S.E., Beauchamp, B., 2009. Latest Permian to Early Triassic basin-to-shelf anoxia in the Sverdrup Basin, Arctic Canada. Chem. Geol. 264 (1–4), 232–246.
Grice, K., Cao, C., Love, G.D., Böttcher, M.E., Twitchett, R.J., Grosjean, E., Summons, R.E., Turgeon, S.C., Dunning, W., Jin, Y., 2005. Photic zone euxinia during the Permian-Triassic superanoxic event. Science 307 (5710), 706–709.
Hays, L.E., Beatty, T., Henderson, C.M., Love, G.D., Summons, R.E., 2007. Evidence for photic zone euxinia through the end-Permian mass extinction in the Panthalassic Ocean (Peace River Basin, Western Canada). Palaeoworld 16 (1–3), 39–50.
He, W., Shi, G.R., Xiao, Y., Zhang, K., Yang, T., Wu, H., Zhang, Y., Chen, B., Yue, M., Shen, J., Wang, Y., Yang, H., Wu, S., 2017. Body-size changes of latest Permian brachiopods in varied palaeogeographic settings in South China and implications for controls on animal miniaturization in a highly stressed marine ecosystem. Palaeogeogr. Palaeoclimatol. Palaeoecol. 486, 33–45.
Huang, Y.G., Chen, Z.Q., Wignall, P.B., Zhao, L.S., 2017. Latest Permian to Middle Triassic redox condition variations in ramp settings, South China: pyrite framboid evidence. Geol. Soc. Am. Bull. 129 (1–2), 229–243.
Isozaki, Y., 1997. Permo-Triassic boundary superanoxia and stratified superocean: records from lost deep sea. Science 276 (5310), 235–238.
Joachimski, M.M., Lai, X., Shen, S., Jiang, H., Luo, G., Chen, B., Chen, J., Sun, Y., 2012. Climate warming in the latest Permian and the Permian-Triassic mass extinction. Geology 40 (3), 195–198.
Kato, Y., Nakao, K., Isozaki, Y., 2002. Geochemistry of Late Permian to Early Triassic pelagic cherts from southwest Japan: implications for an oceanic redox change. Chem. Geol. 182 (1), 15–34.
Kiessling, W., Schobben, M., Ghaderi, A., Hairapetian, V., Leda, L., Korn, D., 2018. Pre–mass extinction decline of latest Permian ammonoids. Geology 46 (3), 283–286.
Krystyn, L., Orchard, M., 1996. Lowermost Triassic ammonoid and conodont biostratigraphy of Spiti, India. Albertiana 17, 10–21.
Krystyn, L., Balini, M., Nicora, A., 2004. Lower and Middle Triassic stage and substage boundaries in Spiti. Albertiana 30, 40–53.
Kump, L.R., Pavlov, A., Arthur, M.A., 2005. Massive release of hydrogen sulfide to the surface ocean and atmosphere during intervals of oceanic anoxia. Geology 33 (5), 397–400.
Lau, K.V., Maher, K., Altiner, D., Kelley, B.M., Kump, L.R., Lehrmann, D.J., Silva-Tamayo, J.C., Weaver, K.L., Yu, M., Payne, J.L., 2016. Marine anoxia and delayed Earth system recovery after the end-Permian extinction. Proc. Natl. Acad. Sci. U.S.A. 113 (9), 2360–2365.
Leventhal, J.S., 1983. An interpretation of carbon and sulfur relationships in Black Sea sediments as indicators of environments of deposition. Geochim. Cosmochim. Acta 47 (1), 133–137.
Li, G.S., Wang, Y.B., Shi, G.R., Liao, W., Yu, L.X., 2016. Fluctuations of redox conditions across the Permian-Triassic boundary-new evidence from the GSSP section in Meishan of South China. Palaeogeogr. Palaeoclimatol. Palaeoecol. 448, 48–58.
Mir, A.R., Balaram, V., Ganai, J.A., Dar, S.A., Krishna, A.K., 2016. Geochemistry of sedimentary rocks from Permian-Triassic boundary sections of Tethys Himalaya: implications for paleo-weathering, provenance, and tectonic setting. Acta Geochim. 35 (4), 428–436.
Mundil, R., Ludwig, K.R., Metcalfe, I., Renne, P.R., 2004. Age and timing of the Permian mass extinctions: U/Pb dating of closed-system zircons. Science 305 (5691), 1760–1763.
Nielsen, J.K., Shen, Y., 2004. Evidence for sulfidic deep water during the Late Permian in the East Greenland Basin. Geology 32 (12), 1037–1040.
Ohmoto, H., Goldhaber, M., 1997. Sulfur and carbon isotopes. In: Barnes, H.L. (Ed.), Geochemistry of Hydrothermal Ore Deposits. 3. pp. 517–611.
Orchard, M., Krystyn, L., 1998. Conodonts of the lowermost Triassic of Spiti, and new zonation based on *Neogondolella Sucessions*. Riv. Ital. Paleontol. Stratigr. 104 (3), 341–368.
Payne, J.L., Turchyn, A.V., Paytan, A., Depaolo, D.J., Lehrmann, D.J., Yu, M., Wei, J., 2010. Calcium isotope constraints on the end-Permian mass extinction. Proc. Natl. Acad. Sci. U.S.A. 107 (19), 8543–8548.
Renne, P.R., Zhang, Z., Richards, M.A., Black, M.T., Basu, A.R., 1995. Synchrony and causal relations between Permian-Triassic boundary crises and Siberian flood volcanism. Science 269 (5229), 1413–1416.
Riccardi, A.L., Arthur, M.A., Kump, L.R., 2006. Sulfur isotopic evidence for chemocline upward excursions during the end-Permian mass extinction. Geochim. Cosmochim. Acta 70 (23), 5740–5752.
Schobben, M., Joachimski, M.M., Korn, D., Leda, L., Korte, C., 2014. Palaeotethys seawater temperature rise and an intensified hydrological cycle following the end-Permian mass extinction. Gondwana Res. 26 (2), 675–683.
Schobben, M., Stebbins, A., Ghaderi, A., Strauss, H., Korn, D., Korte, C., 2015. Flourishing ocean drives the end-Permian marine mass extinction. Proc. Natl. Acad. Sci. U.S.A. 112 (33), 10298–10303.
Scotese, C., 2014. Atlas of Middle & Late Permian and Triassic Paleogeographic Maps, Maps 43—48 From Volume 3 of the PALEOMAP Atlas for ArcGIS (Jurassic and Triassic) and Maps 49–52 From Volume 4 of the PALEOMAP PaleoAtlas for ArcGIS (Late Paleozoic): Mollweide Projection. PALEOMAP Project, Evanston, IL.
Seal, R.R., 2006. Sulfur isotope geochemistry of sulfide minerals. Rev. Mineral. Geochem. 61 (1), 633–677.
Shen, S.-Z., Crowley, J.L., Wang, Y., Bowring, S.A., Erwin, D.H., Sadler, P.M., Cao, C.-Q., Rothman, D.H., Henderson, C.M., Ramezani, J., 2011a. Calibrating the end-Permian mass extinction. Science 334 (6061), 1367–1372.
Shen, Y., Farquhar, J., Zhang, H., Masterson, A., Zhang, T., Wing, B.A., 2011b. Multiple S-isotopic evidence for episodic shoaling of anoxic water during Late Permian mass extinction. Nat. Commun. 2 (210), 1–5.
Shen, J., Schoepfer, S.D., Feng, Q.L., Zhou, L., Yu, J.X., Song, H.Y., Wei, H.Y., Algeo, T.J., 2015. Marine productivity changes during the end-Permian crisis and Early Triassic recovery. Earth Sci. Rev. 149, 136–162.
Shen, J., Feng, Q.L., Algeo, T.J., Li, C., Planaysky, N.J., Zhou, L., Zhang, M.L., 2016. Two pulses of oceanic environmental disturbance during the Permian-Triassic boundary crisis. Earth Planet. Sci. Lett. 443, 139–152.
Shukla, A., Bhandari, N., Shukla, P., 2002. Chemical signatures of the Permian-Triassic transitional environment in Spiti Valley, India. In: Koeberl, G., MacLeod, K.G. (Eds.), Catastrophic Events and Mass Extinctions. 356. Geological Society of America Special Papers, pp. 445–454.
Singh, B.P., 2012. How deep was the early Himalayan foredeep? J. Asian Earth Sci. 56, 24–32.
Singh, T., Tiwari, R.S., Vijaya, Ram-Awatar, 1995. Stratigraphy and palynology of Carboniferous-Permian-Triassic succession in Spiti Valley, Tethys Himalaya, India. J. Paleontol. Soc. India 40, 55–76.
Takahashi, S., Yamasaki, S.I., Ogawa, K., Kaiho, K., Tsuchiya, N., 2015. Redox conditions

in the end-Early Triassic Panthalassa. Palaeogeogr. Palaeoclimatol. Palaeoecol. 432, 15–28.
Tuttle, M.L.W., Breit, G.N., Goldhaber, M.B., 2009. Weathering of the New Albany Shale, Kentucky: II. Redistribution of minor and trace elements. Appl. Geochem. 24 (8), 1565–1578.
Wang, Y., Sadler, P.M., Shen, S.Z., Erwin, D.H., Zhang, Y.C., Wang, X.D., Wang, W., Crowley, J.L., Henderson, C.M., 2014. Quantifying the process and abruptness of the end-Permian mass extinction. Paleobiology 40 (1), 113–129.
Wang, L.N., Wignall, P.B., Wang, Y.B., Jiang, H.S., Sun, Y.D., Li, G.S., Yuan, J.L., Lai, X.L., 2016. Depositional conditions and revised age of the Permo-Triassic microbialites at Gaohua section, Cili County (Hunan Province, South China). Palaeogeogr. Palaeoclimatol. Palaeoecol. 443, 156–166.
Wei, H.Y., Algeo, T.J., Yu, H., Wang, J.G., Guo, C., Shi, G., 2015. Episodic euxinia in the Changhsingian (late Permian) of South China: evidence from framboidal pyrite and geochemical data. Sediment. Geol. 319, 78–97.
Wignall, P.B., Newton, R., 2003. Contrasting deep-water records from the Upper Permian and Lower Triassic of south Tibet and British Columbia: evidence for a diachronous mass extinction. PALAIOS 18 (2), 153–167.
Wignall, P.B., Twitchett, R.J., 1996. Oceanic anoxia and the end Permian mass extinction. Science 272 (5265), 1155–1158.
Wignall, P.B., Twitchett, R.J., 2002. Extent, duration, and nature of the Permian-Triassic superanoxic event. In: Koeberl, G., MacLeod, K.G. (Eds.), Catastrophic Events and Mass Extinctions. 356. Geological Society of America Special Papers, pp. 395–413.
Wignall, P.B., Newton, R., Brookfield, M.E., 2005. Pyrite framboid evidence for oxygen-poor deposition during the Permian–Triassic crisis in Kashmir. Palaeogeogr. Palaeoclimatol. Palaeoecol. 216 (3–4), 183–188.
Wignall, P.B., Bond, D.P., Kuwahara, K., Kakuwa, Y., Newton, R.J., Poulton, S.W., 2010. An 80 million year oceanic redox history from Permian to Jurassic pelagic sediments of the Mino-Tamba terrane, SW Japan, and the origin of four mass extinctions. Glob. Planet. Chang. 71 (1), 109–123.
Wignall, P.B., Bond, D.P., Sun, Y., Grasby, S.E., Beauchamp, B., Joachimski, M.M., Blomeier, D.P.G., 2015. Ultra-shallow-marine anoxia in an Early Triassic shallow-marine clastic ramp (Spitsbergen) and the suppression of benthic radiation. Geol. Mag. 153 (2), 316–331.
Wilkin, R., Barnes, H., Brantley, S., 1996. The size distribution of framboidal pyrite in modern sediments: an indicator of redox conditions. Geochim. Cosmochim. Acta 60 (20), 3897–3912.
Williams, J., 2014. Black Shales of the Neo-Tethys: The Geochemical Record of the End-Permian Crisis (Doctoral Dissertation). pp. 466.
Williams, J., Basu, A., Bhargava, O., Ahluwalia, A., Hannigan, R., 2012. Resolving original signatures from a sea of overprint—the geochemistry of the Gungri Shale (Upper Permian, Spiti Valley, India). Chem. Geol. 324, 59–72.
Xie, S., Algeo, T.J., Zhou, W., Ruan, X., Luo, G., Huang, J., Yan, J., 2017. Contrasting microbial community changes during mass extinctions at the Middle/Late Permian and Permian/Triassic boundaries. Earth Planet. Sci. Lett. 460, 180–191.
Zhang, G., Zhang, X., Hu, D., Li, D., Algeo, T.J., Farquhar, J., Henderson, C.M., Qin, L., Shen, M., Shen, D., Schoepfer, S.D., Chen, K., Shen, Y., 2017. Redox chemistry changes in the Panthalassic Ocean linked to the end-Permian mass extinction and delayed Early Triassic biotic recovery. Proc. Natl. Acad. Sci. U.S.A. 114 (8), 1806–1810.
Zhou, W., Algeo, T.J., Ruan, X., Luo, G., Chen, Z.-Q., Xie, S., 2017. Expansion of photic-zone euxinia during the Permian–Triassic biotic crisis and its causes: microbial biomarker records. Palaeogeogr. Palaeoclimatol. Palaeoecol. 474, 140–151.